


RESEARCH

Open Access



# Effects of acute and chronic oxidative stress on the blood–brain barrier in 2D and 3D in vitro models

Tracy D. Chung<sup>1,2</sup>, Raleigh M. Linville<sup>1,2</sup>, Zhaobin Guo<sup>1</sup>, Robert Ye<sup>1,3</sup>, Ria Jha<sup>1,2</sup>, Gabrielle N. Grifno<sup>1,2</sup> and Peter C. Searson<sup>1,2,4\*</sup> 

## Abstract

Oxidative stress is a shared pathology of neurodegenerative disease and brain injuries, and is derived from perturbations to normal cell processes by aging or environmental factors such as UV exposure and air pollution. As oxidative cues are often present in systemic circulation, the blood–brain barrier (BBB) plays a key role in mediating the effect of these cues on brain dysfunction. Therefore, oxidative damage and disruption of the BBB is an emergent focus of neurodegenerative disease etiology and progression. We assessed barrier dysfunction in response to chronic and acute oxidative stress in 2D and 3D in vitro models of the BBB with human iPSC-derived brain microvascular endothelial-like cells (iBMECs). We first established doses of hydrogen peroxide to induce chronic damage (modeling aging and neurodegenerative disease) and acute damage (modeling the response to traumatic brain injury) by assessing barrier function via transendothelial electrical resistance in 2D iBMEC monolayers and permeability and monolayer integrity in 3D tissue-engineered iBMEC microvessels. Following application of these chronic and acute doses in our in vitro models, we found local, discrete structural changes were the most prevalent responses (rather than global barrier loss). Additionally, we validated unique functional changes in response to oxidative stress, including dysfunctional cell turnover dynamics and immune cell adhesion that were consistent with changes in gene expression.

**Keywords:** Blood–brain barrier, Oxidative stress, Brain microvascular endothelial cells, Hydrogen peroxide, Barrier function

## Background

Oxidative stress is caused by an imbalance of reactive oxygen species (ROS) and other oxidants in relation to antioxidant systems that sequester these species to maintain homeostasis [1, 2]. ROS are capable of chemically disrupting the structure of lipids, proteins, and DNA, ultimately damaging cells and tissues, and hence oxidative stress is implicated in a wide variety of diseases and injury in nearly every organ system [3, 4]. Additionally,

oxidative stress and its correlated diseases are often most prominent in the aging population, although environmental cues, such as air pollution and UV exposure, play a significant role in the acceleration of these diseases in all age groups [5–7]. ROS include hydroxyl radicals, superoxide ions, and hydrogen peroxide (H<sub>2</sub>O<sub>2</sub>), which are produced endogenously in homeostasis but become overabundant in oxidative stress [4].

Of particular interest is the role that oxidative stress plays in neurodegenerative diseases (NDD) where increased oxidative stress is linked to severity of disease pathology [8–11]. Biomarkers of oxidative stress (e.g., peroxiredoxins and ubiquinone/ubiquinol) are elevated in individuals with various NDDs including Alzheimer's

\*Correspondence: searson@jhu.edu

<sup>1</sup>Institute for Nanobiotechnology, Johns Hopkins University, 100 Croft Hall, 3400 North Charles Street, Baltimore, MD, USA  
Full list of author information is available at the end of the article



© The Author(s) 2022. **Open Access** This article is licensed under a Creative Commons Attribution 4.0 International License, which permits use, sharing, adaptation, distribution and reproduction in any medium or format, as long as you give appropriate credit to the original author(s) and the source, provide a link to the Creative Commons licence, and indicate if changes were made. The images or other third party material in this article are included in the article's Creative Commons licence, unless indicated otherwise in a credit line to the material. If material is not included in the article's Creative Commons licence and your intended use is not permitted by statutory regulation or exceeds the permitted use, you will need to obtain permission directly from the copyright holder. To view a copy of this licence, visit <http://creativecommons.org/licenses/by/4.0/>. The Creative Commons Public Domain Dedication waiver (<http://creativecommons.org/publicdomain/zero/1.0/>) applies to the data made available in this article, unless otherwise stated in a credit line to the data.

disease, Parkinson's disease, and amyotrophic lateral sclerosis, and are correlated with cognitive impairments [12–14]. In aging and in response to environmental cues, ROS are not only derived from the brain itself, but from systemic exposure [15–18]. Therefore, the blood–brain barrier (BBB) plays a key role in ROS-mediated injury and diseases of the brain. The BBB tightly regulates transport into and out of the brain via tight junctions, transport systems, and efflux proteins, and is thought to be a key link between vascular comorbidities (e.g., coronary artery disease and diabetes) and NDDs, a concept that is commonly referred to as the vascular hypothesis [19–23]. Immunohistochemical staining of post-mortem human brain tissue and in vivo dye-injection studies in mice have found that local disruption of the BBB due to ROS exposure is correlated with inflammation of the surrounding brain tissue in individuals with NDD [24] and in animal models [25]. Importantly, the susceptibility of the BBB to ROS-induced dysfunction may play a key role in initiation and progression of NDDs [26].

However, while the studies described above have been key in establishing the links between oxidative stress, the BBB, and neurodegenerative disease, a detailed and systematic understanding of BBB dysfunction under oxidative conditions is limited. Many studies rely on staining post-mortem tissue (in which functionality cannot be further studied) [24], intrinsic or extrinsic animal studies (in which species-specific differences may dominate) [25, 27, 28], or exposure of 2D cell monolayers to oxidative agents (e.g.,  $H_2O_2$ ) in which microenvironmental cues are absent [20, 29, 30]. In addition, the pathological effects of oxidative stress are dose-dependent, incorporating both concentration and exposure duration, but many studies do not explore these factors. Acute profiles, which represent a shorter but more intense period of oxidative stress, are associated with traumatic brain injury and ischemia–reperfusion in stroke [31, 32]. For example, studies in rat models of cerebral ischemia/reperfusion have shown a sixfold increase in oxidative stress-responsive apoptosis inducing protein (ORAIP) in cerebrospinal fluid within 30 min of injury, then returns to control levels after four hours [33]. On the other hand, chronic profiles, which represent a longer but less intense period of oxidative stress, are more common in neurodegenerative disease and aging [34–37].

Some early studies in chip-based BBB models have also modeled oxidative and nitrosative stress, primarily via prodrugs such as linsidomine or menadione, with a particular focus on rescuing bulk barrier function following concentration-dependent dosing [38, 39]. To advance our understanding on a more granular level, here we utilize human induced pluripotent stem cell (iPSC)-derived brain microvascular endothelial-like cells (iBMECs) in

2D monolayers and 3D tissue-engineered microvessel models of the BBB that recapitulate the physiological geometry, shear cues, and barrier function of native tissue [40, 41] to identify differences in acute and chronic stress responses to the physiologically-produced ROS hydrogen peroxide ( $H_2O_2$ ). In vitro models were exposed to  $H_2O_2$  concentrations spanning three orders of magnitude across short and long exposure times to identify chronic and acute profiles for further study. These representative profiles resulted in the generation of discrete, local defects which are easily identifiable in tissue-engineered iBMEC microvessels with high spatiotemporal resolution. Additional transcriptomic and functional assessments of these profiles indicated cell cycle disruption and inflammatory immune cell responses that are unique to either chronic or acute oxidative stress. These studies deepen our insight into the dynamic role of oxidative stress in injury and disease of the BBB.

## Materials and methods

### Cell culture

Human induced pluripotent stem cell-derived brain microvascular endothelial-like cells (iBMECs) recapitulate key properties of human BMECs, including expression of tight junctions, efflux pumps, and nutrient transporters [42, 43]. Differentiation of iBMECs was performed as previously reported [44]. iBMECs were differentiated from three isogenic iPSC cell lines from a healthy donor (Allen Cell Collection, WTC parent), that express fluorescently-labeled zona occludens-1 (ZO1), beta-actin (ACTB), and plasma membrane, which produce iBMECs with near-identical morphology and transendothelial electrical resistance [39]. After eleven days of differentiation, iBMECs were detached using Accutase (Thermo Fisher Scientific, A1110501) and seeded onto Transwell inserts or type I collagen microvessel channels coated with  $50 \mu\text{g mL}^{-1}$  human placental collagen IV (Sigma-Aldrich, cat. no. C5533) and  $25 \mu\text{g mL}^{-1}$  fibronectin from human plasma (Sigma Aldrich, cat. no. F2006). During seeding and for the following 24 h, cells were cultured in BBB induction medium composed of human endothelial cell serum-free medium (HESFM) (Thermo Fisher Scientific, cat. no. 11111044) supplemented with 1% human serum from platelet-poor plasma (Sigma-Aldrich, cat. no. P2918), 1% penicillin–streptomycin (Thermo Fisher Scientific, cat. no. 15140122),  $2 \text{ ng mL}^{-1}$  human recombinant basic fibroblast growth factor (bFGF; Fisher Scientific, cat. no. 233FB025CF), and  $10 \mu\text{M}$  all-trans retinoic acid (Sigma-Aldrich, cat. no. R2625). For 24 h before  $H_2O_2$  exposure, cells were further cultured in BBB maintenance medium: HESFM supplemented with 1% human serum from platelet-poor plasma and 1% penicillin–streptomycin.

In 2D Transwell and 3D microvessel experiments, iBMECs were exposed to different concentrations of hydrogen peroxide ( $\text{H}_2\text{O}_2$ ) for 1 h (acute) or over a period of 10 days (chronic). Different concentrations of  $\text{H}_2\text{O}_2$  were prepared by diluting the stock solution (Sigma Aldrich, H1009) in BBB maintenance medium. In all experiments, we define the exposure as the initial concentration at the beginning of the experiment. To determine the concentration profile of  $\text{H}_2\text{O}_2$  in medium over time, we measured  $\text{H}_2\text{O}_2$  levels using the Amplex Red Hydrogen Peroxide Kit (Thermo Fisher, A22188).

#### Transwell-based TEER, cell count, and ROS assays

Transwell inserts (Corning, cat. no. 3470) were coated with  $50 \mu\text{g mL}^{-1}$  collagen IV and  $25 \mu\text{g mL}^{-1}$  fibronectin overnight at  $37^\circ\text{C}$ , then seeded with iBMECs in BBB induction medium at  $1 \times 10^6$  cells  $\text{cm}^{-2}$ . After 24 h, the medium was switched to BBB maintenance medium and daily transendothelial electrical resistance (TEER) measurements were performed using an EVOM-2 and STX-100 electrodes (World Precision Instruments, Sarasota, FL). TEER measurements were recorded daily before initiating experiments or changing medium; monolayers with  $\text{TEER} > 1500 \Omega \text{ cm}^2$  during the 24 h of culture in BBB maintenance media (day 0) were used for experiments. Three experimental conditions were distributed across Transwell inserts: (1) control in BBB maintenance medium without any media switches (control), (2) exposure to sterile water (vehicle), or (3) exposure to various concentrations of  $\text{H}_2\text{O}_2$ . All exposures were conducted by adding  $5 \mu\text{L}$  of water or  $\text{H}_2\text{O}_2$  to the apical chamber (representing a  $20 \times$  dilution). For chronic exposure, confluent monolayers in Transwells were treated with  $\text{H}_2\text{O}_2$  on day 0 and TEER was measured daily for ten days with no media changes. For acute exposure, confluent monolayers in Transwells were treated with  $\text{H}_2\text{O}_2$  on day 0 for 30–60 min, and then the media was replaced with fresh BBB maintenance medium (no  $\text{H}_2\text{O}_2$ ); TEER was then measured every hour for the four subsequent hours and also daily for ten days. All TEER values are reported after subtracting the value for a blank transwell and correcting for the insert area.

To measure intracellular ROS levels and cell counts, monolayers on inserts were washed twice with phosphate buffered saline (PBS; Gibco, 10010049) and treated with Cellular Reactive Oxygen Species Detection Assay Kit (Deep Red Fluorescence) (Abcam, ab186029) according to manufacturer protocols and  $40 \mu\text{g mL}^{-1}$  DAPI solution (Sigma-Aldrich, D9542), respectively. These measurements were conducted at various time points after seeding (days 1, 2, and 4) following a one-hour incubation at  $37^\circ\text{C}$ . Images were collected via epifluorescence on an inverted microscope (Nikon Eclipse TiE) using

a  $4 \times$  objective and NIS Advanced Research software (Nikon). The resultant images were processed using CellProfiler, utilizing built-in modules of illumination correction and identification of primary objects to yield cell count, and utilizing mask generation of cell areas and measuring corresponding intensities to yield ROS signal per cell [45].

#### Tissue-engineered BBB model

Three-dimensional in vitro blood–brain barrier microvessels were generated as previously reported [46]. Briefly, polydimethylsiloxane (PDMS; Dow Corning, 4019862) housings were molded with a cavity for hydrogel patterning and plasma-bonded to glass slides. Utilizing a  $150 \mu\text{m}$  diameter nitinol wire (McMaster-Carr, 8320K12), 1 cm long channels (total surface area of  $\sim 0.05 \text{ cm}^2$ ) were patterned in a rectangular prism of  $7 \text{ mg mL}^{-1}$  type 1 collagen (Corning, 354249). Wires were then removed from the hydrogel leaving an empty channel. 20 mM genipin (Wako Biosciences, MFCD00888600) was perfused through channels for two hours to stiffen collagen and increase cell adhesion [46]. Channels were incubated with matrix proteins ( $50 \mu\text{g mL}^{-1}$  type IV collagen and  $25 \mu\text{g mL}^{-1}$  fibronectin), and seeded with iBMECs suspended in BBB induction medium, supplemented with  $10 \mu\text{M}$  Rho-associated protein kinase (ROCK) inhibitor Y27632 (ATCC, ACS-3030) at a concentration of  $5 \times 10^6$  cells  $\text{mL}^{-1}$  under extremely low-flow conditions ( $\sim 0.01 \text{ mL h}^{-1}$ ) and allowed to adhere for 30 min before initiation of perfusion. Sterile, chemically inert, and noncytotoxic reservoirs (Fisher Scientific, 14-817-32) were connected to both inlet and outlet ports. Perfusion through the vessel was established by filling the upstream reservoir with medium to a height of 5 cm, resulting in a volumetric flow rate of  $\sim 0.5 \text{ mL h}^{-1}$ . The channels were perfused with BBB induction medium supplemented with ROCK inhibitor for 24 h, resulting in the formation of confluent microvessels, and then switched to BBB maintenance medium, and maintained under steady flow. After 24 h in BBB maintenance medium, confluent microvessels were perfused with BBB maintenance medium supplemented with  $100 \mu\text{M}$   $\text{H}_2\text{O}_2$  continuously (chronic exposure), perfused with BBB maintenance medium supplemented with  $500 \mu\text{M}$   $\text{H}_2\text{O}_2$  for one hour followed by perfusion with unsupplemented BBB maintenance medium (acute exposure), or corresponding vehicle control.

To ensure that oxygen depletion during perfusion of the microvessels did not contribute to oxidative stress, we measured the levels of dissolved oxygen in the medium in the inlet reservoir and in the perfusate from the outlet over 5 days using a dissolved oxygen probe (RCYAGO, DO9100).

### Measurement of permeability and identification of defects

To assess changes in permeability and defect formation, microvessels were perfused with two fluorescent solutes: 2  $\mu\text{M}$  Alexa Fluor647-conjugated 10 kDa dextran (Thermo Fisher Scientific, cat. no. D22914) and 200  $\mu\text{M}$  Lucifer yellow (LY; Sigma, CH dilithium salt) in BBB maintenance medium. Microvessels were then imaged (Nikon Eclipse TiE) at  $10\times$  magnification and maintained in an environmental chamber at  $37^\circ\text{C}$ . Epifluorescence illumination was controlled by X-Cite 120LEDBoost (Excelitas Technologies). Phase contrast images (assembled from images from 10 adjacent frames) were acquired every two minutes at the longitudinal top plane, midplane, and bottom plane of the microvessel; fluorescence images were acquired every 2 min at the microvessel midplane. Microvessels were imaged for 10 min before and 1 h following perfusion with the fluorescent solutes.

Three types of structural defects were identified manually by assessing each cropped phase and fluorescent image: (1) delaminations with no focal leak, (2) focal leaks with no delamination, and (3) combination focal leaks and delaminations. Delaminations were identified from phase images where the midplane of the vessel endothelium showed detachment from the channel wall, focal leaks were identified from fluorescence images where there was visible localized leakage of fluorescent solute from the vessel lumen, and combined defects were identified by overlaying the phase and fluorescent images. The time to defect resolution was determined by monitoring fluorescent solute leakage over image sequences.

### Bulk RNA-sequencing and gene set enrichment analysis

RNA was collected from 2D monolayers of iBMECs seeded onto Transwells in the presence of ROCK inhibitor, to match experimental conditions used in tissue-engineered iBMEC microvessels. Collection occurred immediately or four days after acute (500  $\mu\text{M}$ ) exposure to  $\text{H}_2\text{O}_2$  for 1 h and their corresponding vehicle controls, or seven days after initiation of chronic (100  $\mu\text{M}$ ) exposure to  $\text{H}_2\text{O}_2$  and its corresponding vehicle control. Cells were washed with PBS and then lysed using RLT buffer supplemented with 1%  $\beta$ -mercaptoethanol (Sigma, M3148). RNA was purified using the RNeasy Mini Kit (Qiagen) with DNase I digestion, and eluted in RNase-free water, following kit protocols. All sequencing was performed by Novogene on an Illumina NovaSeq platform with paired end 150 bp reads, generating approximately 20 million paired reads per sample. cDNA libraries were constructed following oligo (dT) capture and enrichment. All samples had an RNA integrity number  $> 8.8$  (Agilent 2100 Bioanalyzer).

Raw read alignment and quantification to the reference human genome (GRCh38) was performed using the R

(v4.0.1) package Rsubread (v2.0.1) [48]. Normalization, visualization, and differential analysis was performed using the R package DESeq2 (v1.28.1) [49]. Normalization of raw reads in DESeq2 utilized variance stabilizing regularized logarithm transformation (rlog) before calculation of Euclidean sample distances and resultant principal component analysis (PCA). Differentially expressed genes (DEGs) were identified using the Wald test with Benjamini–Hochberg correction-adjusted p-values, where values  $< 0.05$  were considered statistically significant. Gene set enrichment analysis was conducted by inputting an enriched set of genes, composed of all DEGs and genes with  $> 3 \log_2\text{FC}$ , into Enrichr and assessing GO biological processes and MSigDB Hallmark pathways [50]. Visualizations (PCA, volcano plots) were formatted using R package ggplot2 (v3.3.2) [51].

### Cell turnover analysis

Cell loss and mitosis events in microvessels were counted manually from phase contrast imaging sequences acquired every 2 min over 1 h. The total number of iBMECs were counted manually from the polar planes of the microvessel, then cell loss and mitosis events were observed manually, as reported previously [39]. Briefly, cell loss events were identified by an appearance of cell swelling and disappearance from the monolayer. Mitosis events were identified by observing cell compression and formation of daughter cells. The rate of turnover was calculated from the difference between the rates of mitosis and cell loss, and is presented as a percentage of all cells per hour ( $\% \text{h}^{-1}$ ).

### Immune cell adhesion

Immune cell adhesion assays were conducted at days 1 and 4 after  $\text{H}_2\text{O}_2$  exposure in a tissue-engineered microvessel. Human THP-1 cells, a monocytic cell line derived from an acute monocytic leukemia patient, were cultured in RPMI-1640 medium (Thermo Fisher Scientific, 11875093) supplemented with 10% fetal bovine serum (Sigma, F4135) and 1% penicillin–streptomycin (Thermo Fisher Scientific, cat. no. 15140122). An expanded stock of THP-1s were frozen in liquid nitrogen and thawed 24 h prior to use. Before each experiment, THP-1s were suspended in serum-free RPMI-1640 medium and incubated for 20 min with CellTracker Deep Red (Thermo Fisher Scientific, C34565) according to product protocols. After washing the cells twice with PBS, THP-1s were resuspended at a final concentration of  $1 \times 10^6$  cells  $\text{mL}^{-1}$  and 70  $\mu\text{L}$  of this suspension (70,000 cells) was perfused through the device for 10 min under low shear stress ( $\sim 0.2$  dyne  $\text{cm}^{-2}$ ). Afterwards, any remaining cell suspension upstream of the device was removed and replaced with BBB maintenance medium



to wash out non-adherent THP-1s for 20 min. Adherent fluorescently-labeled THP-1s were manually counted in each device, and normalized to microvessel length.

**Statistical analysis**

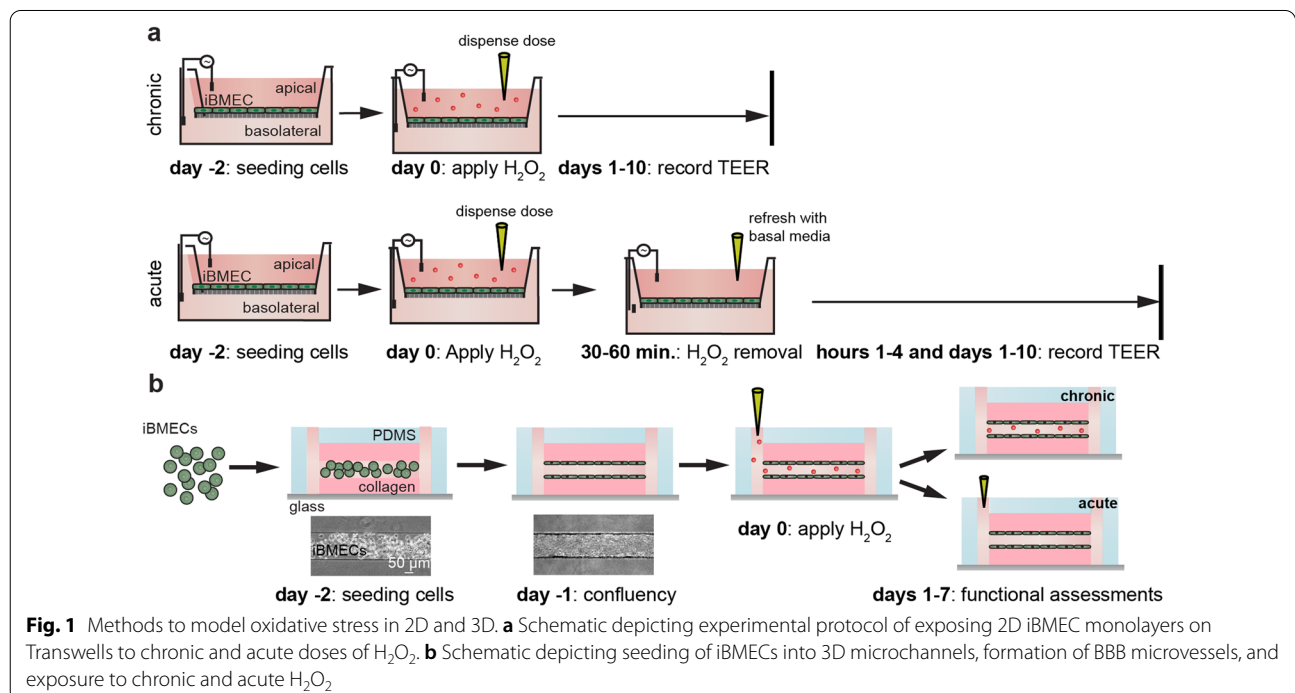
Biological replicates are defined as experiments conducted with an independent differentiation of iBMECs. All statistical analysis was performed using Prism 9 (GraphPad). All data are presented as mean ± SEM (standard error of the mean). A student’s unpaired *t*-test (two-tailed with unequal variances) was used for comparison of two groups and an analysis of variance (ANOVA) was used for comparisons of three or more groups. Tukey’s multiple comparisons test was used to compare experimental conditions across groups of three or more, where reported *p*-values were multiplicity adjusted. Statistical significance was defined at *p* < 0.05, with \**p* < 0.05, \*\**p* < 0.01, and \*\*\**p* < 0.001.

**Results**

Neurodegenerative diseases and brain injuries are associated with acute or chronic exposure to oxidative stress. Since there are no established protocols for modeling oxidative stress exposure, we first determined conditions for acute and chronic injury of iBMEC monolayers to the ROS hydrogen peroxide (H<sub>2</sub>O<sub>2</sub>). H<sub>2</sub>O<sub>2</sub> is a commonly studied oxidative agent used in vitro due to its capacity to mimic oxidative stress by stimulating hydroxyl radical formation and its relative stability in

cell culture medium [52]. A key challenge for in vitro studies is modeling a pathological response to mimic human disease and injury. Results from animal studies have indicated that baseline levels of H<sub>2</sub>O<sub>2</sub> may be around 50 μM, although following injury, such as ischemia–reperfusion in the striata of rat brains, levels may increase to 200 μM [53]. Although there have been relatively few studies of cytotoxic exposure to H<sub>2</sub>O<sub>2</sub> in humans, levels of systemic irritation are known to occur at around 100 μM when inhaled and 10 mM when ingested, which provide benchmarks for exposure in our model systems [54–56]. Based on these observations, we sought to establish models of chronic and acute oxidative stress exposure in 2D iBMEC monolayers on Transwells (Fig. 1a) and in 3D tissue-engineered iBMEC microvessels (Fig. 1b).

To establish dose regimes leading to physiological, pathological, and cytotoxic responses, iBMEC monolayers in Transwells and microvessels were exposed to concentrations of H<sub>2</sub>O<sub>2</sub> from 10 μM to 10 mM for durations of up to 1 h (acute exposure) or up to 10 days (chronic exposure). From independent measurements of the H<sub>2</sub>O<sub>2</sub> concentration in cell culture over time, we found that the concentration of H<sub>2</sub>O<sub>2</sub> decreased over several days (Additional file 1: Fig. S1). Therefore, the H<sub>2</sub>O<sub>2</sub> concentration in acute exposure is approximately constant, whereas in chronic exposure the H<sub>2</sub>O<sub>2</sub> levels decrease over time, more significantly after 5 days of culture.



**In vitro measurements recapitulate acute and chronic oxidative stress profiles**

To establish the influence of H<sub>2</sub>O<sub>2</sub> dose on barrier function, we first assessed changes in TEER in 2D confluent monolayers of iBMECs (Fig. 2a, b). In agreement with previous human exposure studies, continuous exposure to 10 μM or 100 μM resulted minimal changes in TEER over 10 days (Fig. 2a). Continuous exposure to 1 mM H<sub>2</sub>O<sub>2</sub> resulted in a gradual decrease in TEER

over several days, with values below 500 Ω cm<sup>2</sup> on day 9 after exposure (\**p* = 0.018 vs. vehicle). TEER values for iBMECs below 500 Ω cm<sup>2</sup> are associated with increased solute permeability [57]. Acute doses probed the interactions between H<sub>2</sub>O<sub>2</sub> concentration and exposure duration, spanning 1 mM to 10 mM exposure for either 30 or 60 min (Fig. 2b). An exposure of 1 mM H<sub>2</sub>O<sub>2</sub> for one hour resulted in a gradual decrease in TEER beginning on day two and decreasing to 700 Ω cm<sup>2</sup> over 10 days,

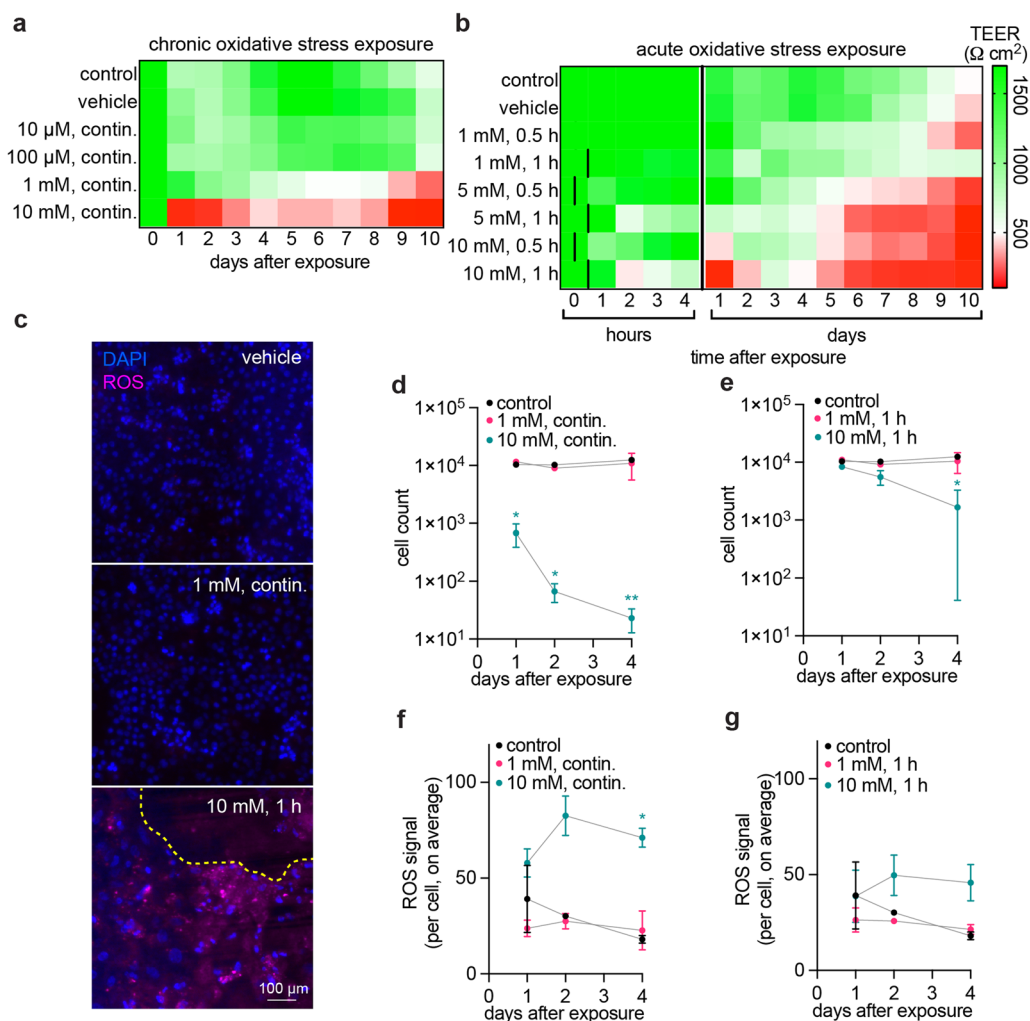


**Fig. 2** Dose-dependent response of 2D iBMEC monolayers to chronic and acute oxidative stress. **a** Heatmap of iBMEC TEER during chronic exposure to H<sub>2</sub>O<sub>2</sub> at various concentrations and corresponding controls (no addition, or vehicle addition). Continuous 1 mM H<sub>2</sub>O<sub>2</sub> exposure resulted in a gradual loss of barrier function over 10 days that models chronic oxidative stress. Each cell represents the mean of three technical replicates across *n* = 3 biological replicates in all conditions. **b** Heatmap of iBMEC TEER during acute exposure to H<sub>2</sub>O<sub>2</sub> at various concentrations and exposure times and corresponding controls (no addition, or vehicle addition). 10 mM H<sub>2</sub>O<sub>2</sub> exposure for one hour resulted in significant but recoverable loss of barrier function over 10 days that is consistent with acute oxidative stress. Each cell represents the mean of three technical replicates across *n* = 7 biological replicates in all conditions. **c** Representative images from DAPI and ROS assay staining showing the negative control with minimal ROS accumulation, continuous 1 mM H<sub>2</sub>O<sub>2</sub> exposure with minimal ROS accumulation, and acute 10 mM H<sub>2</sub>O<sub>2</sub> exposure with visible ROS accumulation and cell loss. Yellow dotted line indicates a region of cell loss (no nuclei). **d, e** Quantification of cell counts over time following chronic and acute exposure, respectively. **f, g** Quantification of intracellular ROS per cell over time following chronic and acute exposure, respectively. Statistical tests were conducted versus control at each timepoint. *n* = 3 biological replicates for all conditions and time courses for (**d–g**)

but not significantly different from control conditions (ns,  $p=0.836$ ). However, a ten-fold increase in concentration to 10 mM  $H_2O_2$  for one hour dramatically decreased TEER within three hours ( $*p=0.013$  vs. vehicle), with values remaining low for the following two days ( $*p=0.036$  vs. vehicle), before returning to values similar to controls on day three following exposure (ns,  $p=0.633$  vs. vehicle). This profile is consistent with acute and reversible damage that recovers over several days. To understand the role of cellular damage in these TEER studies, we further investigated cell counts and intracellular ROS levels (Additional file 1: Fig. S2c–g). While measurable ROS levels were correlated with macroscopic and functional disruption of the monolayer, oxidative stress responses were below the detection limit of the assay. These observations are exemplified in representative images of a negative vehicle control, 1 mM chronic  $H_2O_2$  exposure that produced no measurable ROS but resulted in TEER loss, and 10 mM acute  $H_2O_2$  exposure that resulted in measurable ROS and significant cell loss (i.e., toxicity) (Fig. 2c). Cell counts remained unchanged in chronic and acute exposure to 1 mM  $H_2O_2$ , but resulted in dramatic decreases in cell count during continuous 10 mM exposure ( $*p=0.018$ ,  $0.016$ , and  $**p=0.001$  vs. control at days 1, 2, and 4, respectively), and significant decrease in cell count by day 4 in acute one-hour 10 mM exposure ( $*p=0.032$  vs. control) (Figs. 2d, e). ROS accumulation was measured using a fluorescent detection kit and followed similar trends to cell count (Additional file 1: Fig. S1e, f). Chronic and acute 1 mM  $H_2O_2$  exposure produced no measurable change in ROS accumulation, but continuous 10 mM exposure resulted in a significant increase in ROS by day four ( $*p=0.022$  vs. control) (Fig. 2f). Acute one-hour 1 mM  $H_2O_2$  exposure resulted in slight increases in ROS, but not at a significant level ( $p=0.117$  vs. control at day 4) (Fig. 2g). In summary, ROS were detected only at cytotoxic exposures associated with significant cell loss from the monolayer. At lower concentrations, we observed decreased TEER values but the sensitivity of the assay was not sufficient to detect increases in ROS.

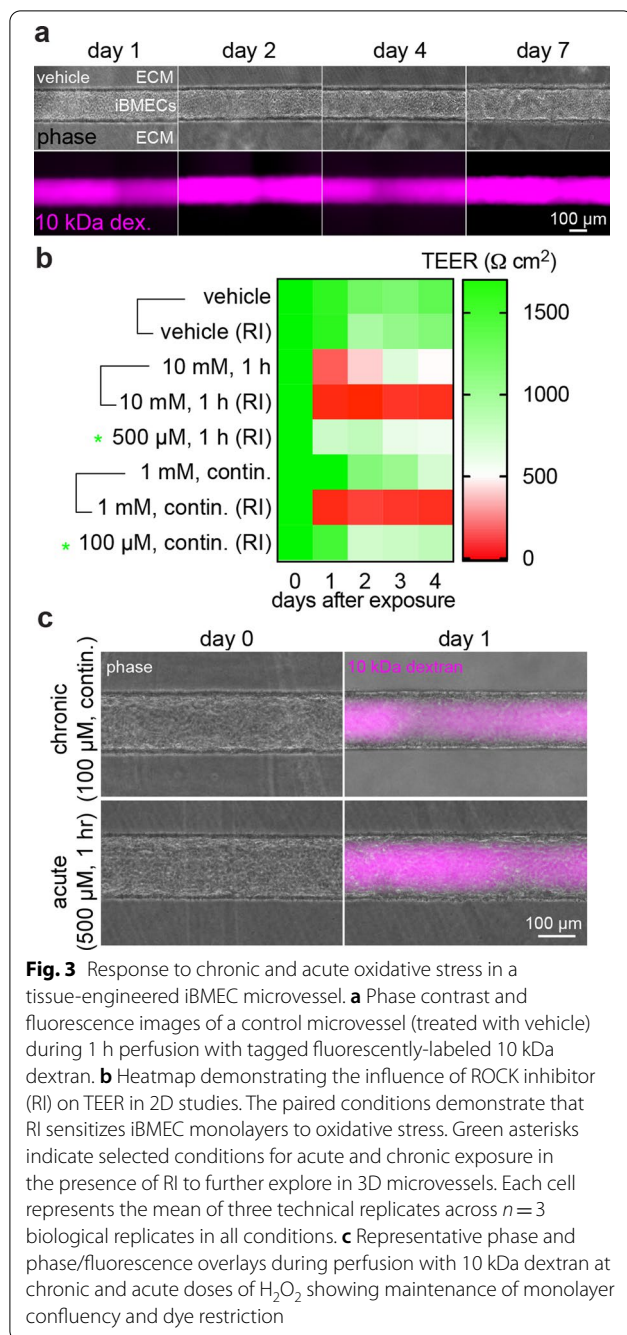
Together, these results are consistent with competition between homeostatic forces, stress exposure, and the capacity of antioxidants to regulate ROS accumulation and promote proliferation to maintain a confluent monolayer. There are three key parameters in selecting dosing conditions to model chronic and acute oxidative stress: (1) exposure should be below previously documented concentrations that trigger systemic irritation (which includes presentation of burning of the eyes or skin, itching and dryness in the throat, cough, and a variety of other symptoms) in humans (10 mM), (2) exposure should recapitulate measurable barrier dysfunction, and

(3) exposure should not result in significant cell death. Therefore, the dosing range of the perturbation should lie in a “pathological” regime: maintenance of relatively high cell viability but sustaining some loss of barrier function. The pathological response should be between “physiological” (maintenance of high cell viability and no evidence of loss of barrier function) and “cytotoxic” (very low cell viability with significant loss of barrier function). Our 2D experiments suggest that the pathological stress regime, prior to the onset of cytotoxicity, may be relatively narrow in vitro; thus, we selected the following conditions to model acute and chronic oxidative stress exposure: (1) chronic oxidative stress: continuous 1 mM  $H_2O_2$  exposure, resulting in a gradual decrease in TEER, and (2) acute oxidative stress: a one-hour exposure to 10 mM  $H_2O_2$ , resulting in a short-term decrease and partial recovery in TEER.

### Three-dimensional models reveal discrete, local defects in response to oxidative stress

To model oxidative stress in a system mimicking the physiological cues of the BBB microenvironment, we next performed experiments in a tissue-engineered iBMEC microvessel model perfused with culture media supplemented with  $H_2O_2$  (Fig. 1b). Microvessels maintained barrier function for at least one week as previously reported [40], and remained confluent over at least seven days after maturation with no focal leaks (Fig. 3a). The 3D microenvironment and cell culture conditions maintained normal oxygen exchange and cellular respiration. The dissolved oxygen in the inlet reservoir was on average 17.7%, close to the expected value of 18.6% under normal cell culture conditions (5 vol.%  $CO_2$  and 37 °C) (Additional file 1: Fig. S3) [47]. The concentration in the outlet perfusate was on average 16.8%, indicating a ~0.9% drop in dissolved oxygen due to cell metabolism during perfusion. However, there are two major differences between 2D and 3D culture conditions relevant to oxidative stress exposure. First, 3D microvessels are continually perfused with ROS in comparison to monolayers in 2D Transwells. Second, 3D microvessels are perfused with medium supplemented with Rho-associated protein kinase (ROCK) inhibitor (Y27632) during seeding and the first 24 h of perfusion (to enhance cell adhesion and spreading). Therefore, expected conditions to recapitulate acute and chronic stress exposure are different in 3D than in 2D systems (Additional file 1: Fig. S4a, b).

To determine these different exposures, we conducted additional experiments in 2D monolayers to evaluate the influence of ROCK inhibitor on iBMEC responses to oxidative stress (Fig. 3b). When added to the media in Transwells prior to  $H_2O_2$  exposure, ROCK inhibitor resulted in a significant decrease in TEER; therefore,



reduced  $H_2O_2$  doses best recapitulated chronic and acute oxidative stress dynamics given these culture conditions (Fig. 3b, Additional file 1: Fig. S4c). In 3D, these corresponding reduced  $H_2O_2$  doses resulted in confluent monolayers and minimal change in global permeability immediately following exposure (Fig. 3c). However, local dysfunction emerged on longer time-scales, which we

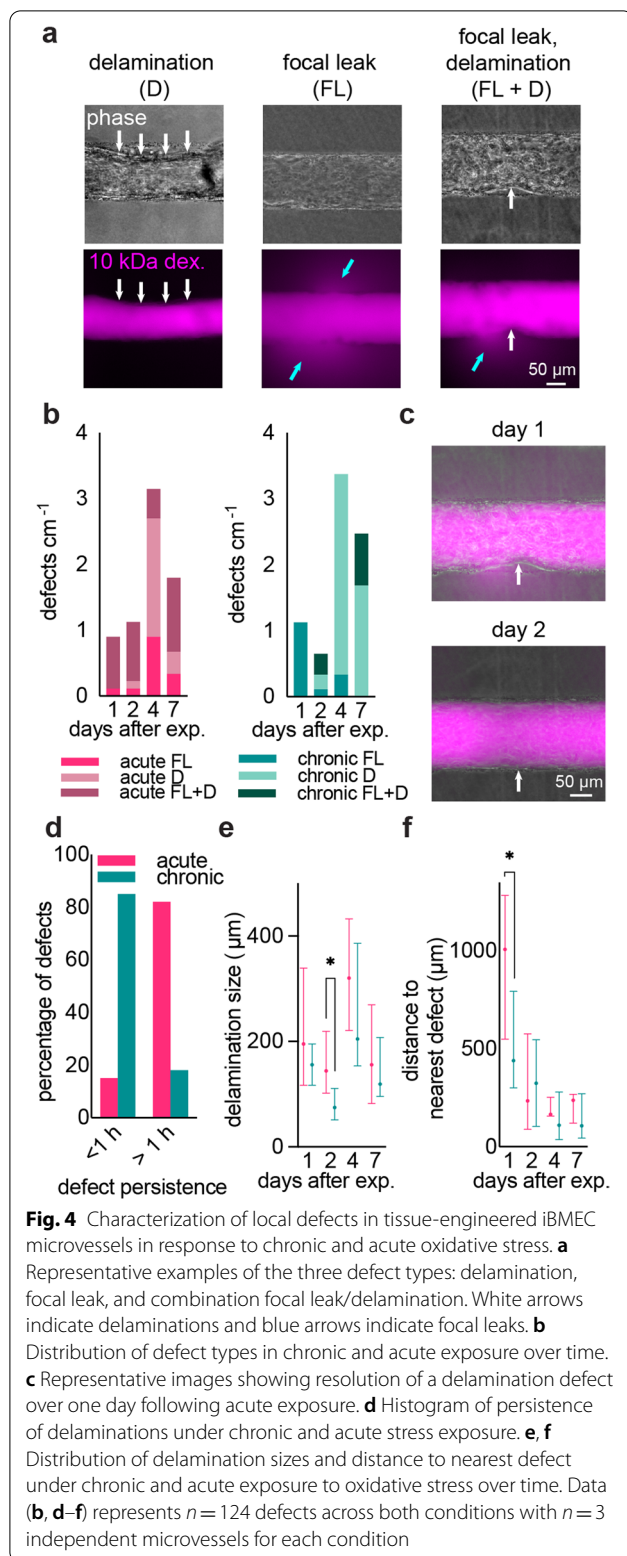
explored by perfusion with fluorescently tagged 10 kDa dextran and Lucifer yellow (MW 444.24 Da).

From phase contrast images and fluorescence images, we found that discrete, local defects dominated over global changes to permeability. Defects were characterized as focal leaks, delaminations (local loss of adhesion), or combination focal leaks with delaminations (Fig. 4a). All three types of defects were observed with both chronic and acute exposure, and the number of unique defects increased with time (Fig. 4b). Comparing chronic and acute exposure, combination focal leak/delaminations were more prevalent in acute conditions, with this trend becoming more significant over time ( $**p = 0.005$  at day 4,  $***p < 0.001$  at day 7). Additionally, while the distribution of defect type within acute conditions did not favor a particular defect classification, chronic conditions resulted in significantly more delaminations than focal leaks or combination focal leak/delaminations, with the comparative significance peaking at day 4 after exposure ( $**p = 0.007$  for delaminations vs. focal leaks,  $**p = 0.008$  for delaminations vs. combination focal leak/delaminations). While defect distribution was dependent on oxidative stress condition, in confluent regions away from defect sites, the local permeability of fluorescent solutes was largely unchanged (Additional file 1: Fig. S5), which indicates that discrete defects are the primary sites of dysfunction and that barrier function elsewhere in the microvessels is unaffected.

From daily imaging of microvessels we observed that all three types of defects had the potential for recovery (Fig. 4c). Delaminations resolved by re-adherence of the endothelium to the ECM, while focal leaks resolved by reversal of dye leakage. To understand the time course of this recovery, we defined the persistence as the duration of time between the appearance of the defect and re-adherence (for delaminations) and resolution of dye leakage (for focal leaks). Acute exposure resulted in increased persistence of defects, whereas chronic exposure resulted in defects that typically recovered on the order of minutes (Fig. 4d).

Delaminations were generally larger and exhibited a broader range of sizes following acute exposure. Chronic exposure resulted in smaller delaminations (with the difference between conditions peaking at day 2), although the range of sizes increased with time (Fig. 4e). Defect clustering was assessed from the distance to the nearest defect and, for both acute and chronic exposure, delaminations became more clustered several days after initial exposure, with the only significant difference occurring one day after exposure (Fig. 4f).



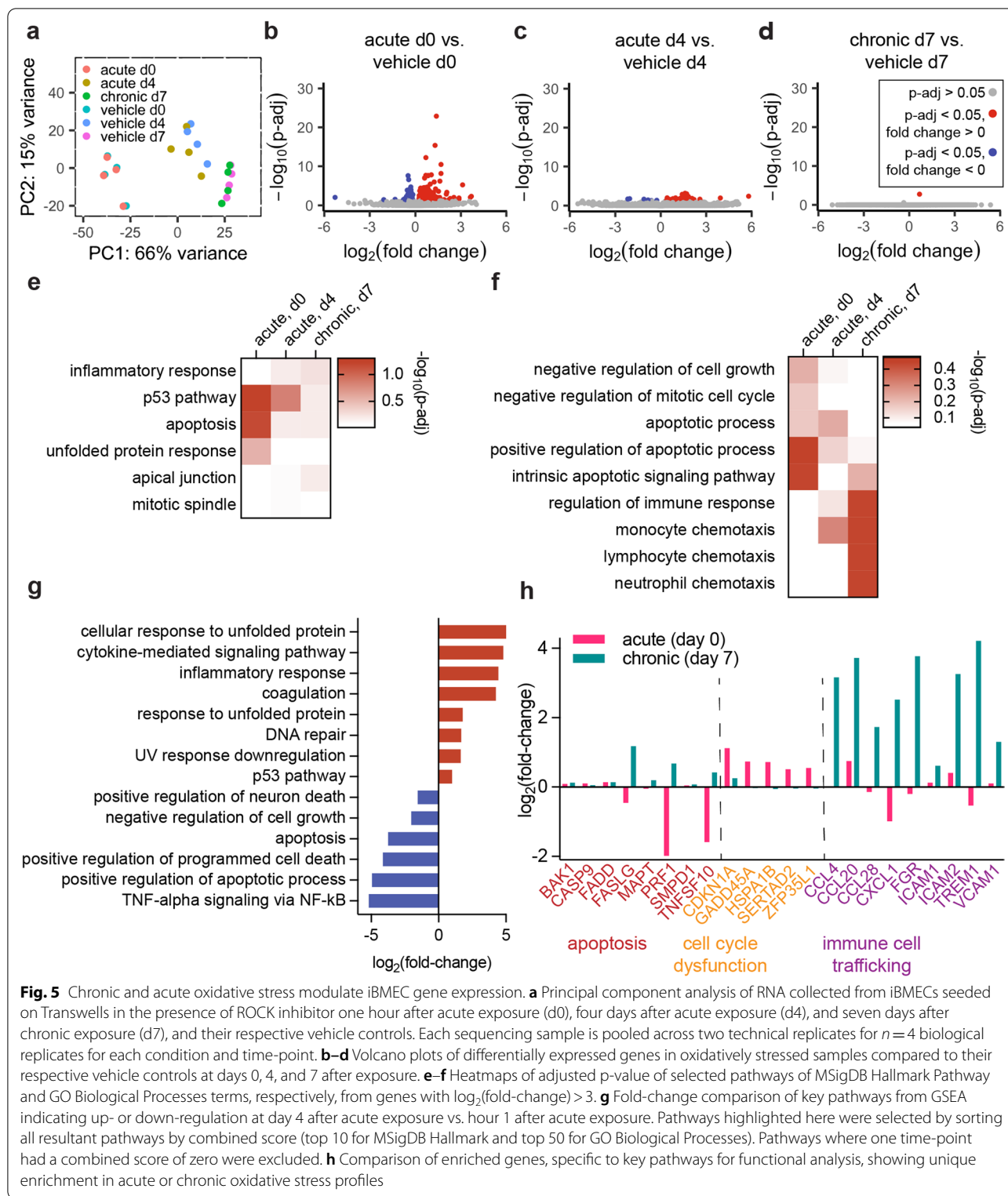


**Bulk RNA-sequencing highlights upregulation of inflammatory pathways following oxidative stress**  
 Having characterized the structural changes that lead to

loss of barrier function, we next assessed gene expression to identify other aspects of BBB function altered by oxidative stress. To simultaneously verify barrier function via TEER measurements (Additional file 1: Fig. S6a), and to collect enough nucleic acid material for sequencing, 3D exposure conditions were matched in 2D Transwell conditions and 3D iBMEC microvessels were utilized to validate and visualize oxidative stress responses found in transcriptomic results. iBMECs were seeded in the presence of ROCK inhibitor onto transwells and treated with either control medium, medium supplemented with 100  $\mu\text{M}$   $\text{H}_2\text{O}_2$ , or medium supplemented with 500  $\mu\text{M}$   $\text{H}_2\text{O}_2$  which was then replaced with control medium after one hour (matching 3D conditions explored in Figs. 3 and 4). RNA was collected immediately after acute exposure, four days after acute exposure, and seven days after chronic exposure. In all cases, RNA from control monolayers was collected at identical timepoints for paired comparisons. From principal component analysis of the results, we found that maturation time had a larger effect on gene expression than oxidative stress experimental conditions (Fig. 5a). These results indicate that iBMECs in 2D monolayers undergo substantial phenotypic drift that should be addressed in future work.

To explore differences between oxidative stress conditions, we identified differentially expressed genes (DEGs) (Fig. 5b–d) and conducted gene set enrichment analysis (GSEA) with all genes with a  $\log_2(\text{fold-change}) > 3$  for all experimental conditions (Fig. 5e, f). Immediately after acute exposure we found 175 upregulated and 116 downregulated genes ( $p\text{-adj} < 0.05$ ) compared to the control. Four days after acute exposure, the number of upregulated and downregulated DEGs decreased to 39 and 6, respectively. Interestingly, seven days after chronic exposure, there was only one upregulated gene compared to control. The fold-change of key genes related to the highlighted pathways reflected these patterns: generally, genes related to BBB identity and function were downregulated, while genes related to inflammation, protein breakdown, and immune cell adhesion were upregulated (Additional file 1: Fig. S6b). Selected genes associated with active barrier transport (such as efflux pumps and receptor-mediated endocytosis proteins) were also assessed (Additional file 1: Fig. S6c) and most transporters showed changes in expression levels of  $\log_2(\text{fold-change}) < 1$ .

The top upregulated molecular pathways across all oxidative stress exposures from MSigDB Hallmark (Fig. 5e, Additional file 1: Fig. S6d) and GO Biological Processes families (Fig. 5f, Additional file 1: Fig. S6e) were predominantly associated with inflammation and survival, including shared enriched pathways in both exposure schemes related to programmed cell death (MSigDB: Apoptosis, GO: 0006915, 0043065, 0097193, 0070059, 1902043,



0043281, 0001844, 0043068), p53 pathways (MSigDB: p53 Pathway), and specific inflammatory pathways, including tumor necrosis factor and subsequent NF- $\kappa$ B signaling

(MSigDB: TNF-alpha Signaling via NF- $\kappa$ B, GO: 0071346), which provide important targets for designing assays of these cytokine pathways during BBB dysfunction.

Additionally, key oxidative stress response genes, particularly glutaredoxins and glutathione peroxidases, stress fiber formation genes, and key Intermediate-Early Genes (IEGs) are upregulated among all oxidative stress conditions (Additional file 1: Figs. S7, S8c). Enriched pathways unique to acute oxidative stress included multiple gene sets associated with negative regulation of homeostatic processes and cell cycle arrest (GO: 0032845, 0045926, 0030308, 0045930). Enriched pathways unique to chronic oxidative stress involved immune cell attraction and adhesion (GO: 0050776, 0060099, 0050764, 0050855, 0043304, 0002548, 0048247, 0070098, 0030593, 2000403, 0051133). Both general families of upregulated pathways provide insight into functional changes that were further studied in our *in vitro* system.

Comparison of transcriptomic changes on day four compared to immediately after acute exposure were consistent with observed functional recovery in 2D monolayers two days after exposure to H<sub>2</sub>O<sub>2</sub> (Fig. 5g). A fold-change comparison of top MSigDB Hallmark and GO Biological Processes between four days after exposure and one hour after exposure revealed a time-dependent downregulation in many inflammatory and apoptotic pathways (MSigDB: Apoptosis, TNF-alpha Signaling via NF-kB, GO: 0030308, 0043068, 1901216), and upregulation of cellular stress responses, such as DNA repair (MSigDB: DNA Repair) and coagulation (MSigDB: Coagulation). This shift suggests barrier recovery is concurrent with a decrease in inflammatory responses.

GSEA revealed a number of shared pathways between chronic and acute oxidative stress, but to demonstrate the utility of our *in vitro* models in representing unique modes of dysfunction, we sought pathways that were unique to either exposure profile to pursue in functional assays. Pathway-level comparisons indicated changes in apoptotic, mitotic, and other cell cycle changes were more prevalent in acute oxidative stress, while upregulation of immune cell chemotaxis and migration was more prevalent in chronic oxidative stress. Additionally, families of associated genes for each pathway more specifically reflect these trends (Fig. 5h).

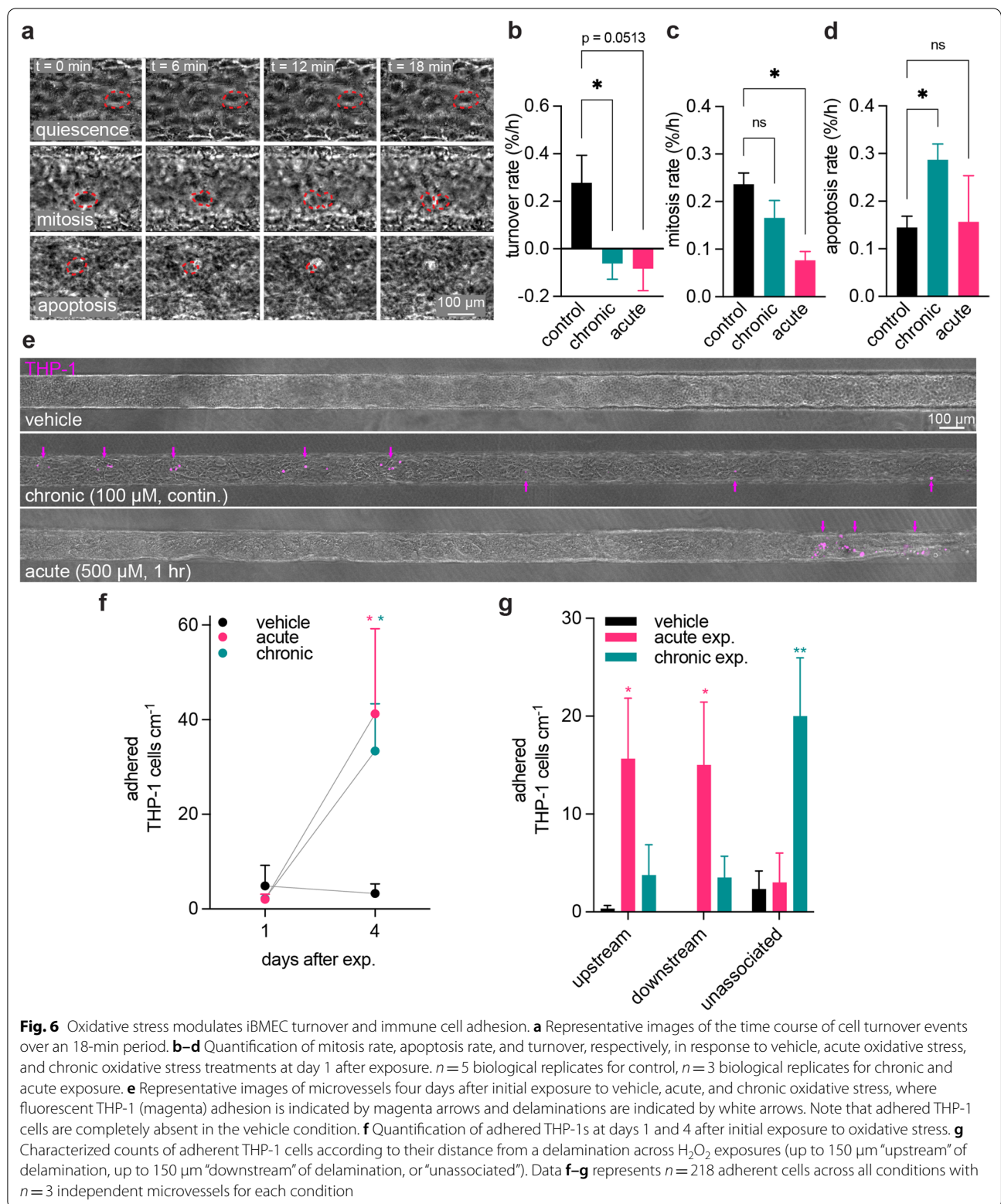
#### Chronic and acute oxidative stress modulate cell turnover and immune cell adhesion

We validated RNA sequencing studies by measuring cell turnover and immune cell adhesion in iBMEC microvessels exposed to oxidative stress. First, to determine cell turnover, we manually identified mitotic and apoptotic events from phase contrast images collected over one hour, one day after exposure (Fig. 6a). Overall, the rates of mitosis and apoptosis were approximately equal in control microvessels, resulting in a net turnover rate of

0.037% per hour. However, both chronic and acute oxidative stress exposure resulted in negative cell turnover rates ( $-0.062\%$  and  $-0.083\%$  per hour, and  $*p=0.038$  and  $p=0.051$ , respectively), indicating a net loss of cells over time (Fig. 6b). Although the turnover rates were similar in response to chronic and acute exposure, the origin of these differences was different. Chronic oxidative stress resulted in a similar mitosis rate to control microvessels, but a higher rate of apoptosis ( $*p=0.047$ ) (Fig. 6c). In contrast, acute oxidative stress resulted in a lower rate of mitosis ( $*p=0.011$ ), but a similar rate of apoptosis compared to controls (Fig. 6d).

Previously published studies of immune cell behavior *in vivo* and *in vitro* primary cell culture have demonstrated a link between inflammatory conditions (such as disease or injury) and increased immune cell recruitment, particularly via adhesion molecules including ICAM-1, VCAM-1, and e-selectin [58–60]. Recent studies in iPSC-derived BBB models found that direct induction of inflammatory conditions with key cytokines can promote upregulation of adhesion molecules and interactions with T cells [61]. To further explore immune cell adhesion in the BBB in the context of oxidative stress as indicated by our transcriptomic results, we perfused microvessels with fluorescently-labeled THP-1 cells, a monocyte-like cell line, one or four days following chronic or acute H<sub>2</sub>O<sub>2</sub> exposure (Fig. 6e). One day following exposure the vehicle control had 4.90 adhered THP-1s cm<sup>-1</sup>, and there were no statistical differences between the number of adherent immune cells across experimental conditions ( $p=0.958$  for acute exposure,  $p=0.954$  for chronic exposure) (Fig. 6f). However, four days after exposure, the number of adherent immune cells increased to 33.4 cm<sup>-1</sup> under chronic oxidative stress ( $*p=0.032$ ) and 41.3 cm<sup>-1</sup> under acute oxidative stress ( $*p=0.012$ ), while control conditions maintained a low level of immune cell adhesion. Although there was no significant difference in the number of adherent immune cells after four days between chronic or acute exposure, the spatial distribution was dependent on the defect type. Adhesion often occurred in the form of clusters, and predominantly upstream of delaminations (Fig. 6e). This was particularly apparent in acute exposure, which tended to result in more delaminations in comparison to chronic exposure.

To quantify this spatial heterogeneity, each adherent THP-1 was categorized based on its upstream or downstream proximity to a delamination (Fig. 6g). THP-1s were defined as proximal if they were within 150  $\mu\text{m}$  “upstream” or “downstream” of the edge of the delamination; and were defined as “unassociated” if they were further than 150  $\mu\text{m}$  from the delamination. Acute exposure resulted in a majority of adherent immune



cells associated (either upstream or downstream) with a delamination ( $*p = 0.035$  vs. control for upstream THP-1s,  $*p = 0.0395$  vs. control for downstream THP-1s). On

the other hand, chronic exposure resulted in a majority of adherent immune cells unassociated with a delamination ( $**p = 0.009$  vs. control). This quantification of



spatial observations indicates potentially different etiologies of immune cell adhesion in response to different oxidative stress exposures. While structural defects and their influence on immune cell residence time during perfusion may dominate in acute oxidative stress, other modalities must influence the increased immune cell adhesion observed in chronic oxidative stress. While it may be hypothesized that adhesion molecule expression may play a role in chronic exposure, immunofluorescence imaging of ICAM-1 and VCAM-1, critical receptors associated with endothelial cell activation that promote immune cell adhesion, four days after exposure to oxidative stress was inconclusive (Additional file 1: Fig. S9). Future detailed analysis of the spatial distribution of activated endothelial cells and the location of adherent immune cells will be necessary to further determine the influence of oxidative stress on this aspect of immune response.

## Discussion

Oxidative stress plays an important role in the progression of brain diseases, including neurodegeneration and traumatic brain injury [8–11]. Sources of ROS that induce oxidative stress are both intrinsic and environmental, and hence BBB dysfunction is at the nexus of disease progression in response to oxidative stress. In the brain, local oxidative stress generated by parenchymal cellular dysfunction or by toxic proteins can induce BBB dysfunction, which can in turn exacerbate neuroinflammation by entry of blood components [27, 62–64]. Systemic ROS resulting from environmental cues can also damage the BBB, leading to vascular dysfunction, the accumulation of toxic proteins, and downstream neuroinflammation [15–18, 24, 25]. While these effects of oxidative stress have been observed globally, many previous studies have been unable to clearly demonstrate the spatiotemporal manifestation of BBB dysfunction under oxidative stress, as most utilize model organisms that limit this resolution or only study continuous exposure to ROS [25, 27, 28]. Thus, to better understand BBB phenotype during oxidative stress exposure, we assessed the response of 2D monolayers and 3D tissue-engineered microvessels to acute and chronic hydrogen peroxide ( $H_2O_2$ ).

$H_2O_2$  is a ROS that is commonly used in experimental studies of oxidative stress, but dosages must be carefully calibrated, as its relative stability allows it to act as a second messenger of redox signaling, typically at very low concentrations (1–10 nM) [65]. At higher concentrations,  $H_2O_2$  is oxidized to more reactive forms, typically the hydroxyl radical that initiates DNA, protein, and lipid damage, leading to oxidative stress [66]. This transition from homeostatic to pathological phenotype was previously studied in 2D monolayers of primary rat

BMECs, where three distinct regimes were found: low concentrations from 1 nM to 1  $\mu M$   $H_2O_2$  which resulted in enhanced angiogenesis, concentrations above 100  $\mu M$  which resulted in increased permeability, and concentrations above 10 mM which resulted in increased apoptosis [29]. Related studies using a bead assay showed that exposure to <1 mM  $H_2O_2$  enhanced angiogenic responses [67]. Our results for iBMECs in 2D are consistent with these thresholds, as in both chronic and acute profiles, the barrier disruptive effects of  $H_2O_2$  were concentration-dependent in a range from 100  $\mu M$  to 10 mM, which is also within the spectrum of physiological to pathological exposure observed in humans [55, 56].

Comparison of the response of iBMEC monolayers in 2D and 3D is complicated by the differences in flow conditions and the influence of ROCK inhibitor. Both effects sensitize endothelial barriers to  $H_2O_2$  exposure. ROCK inhibitor has been demonstrated to exert both protective and detrimental effects on endothelial barrier function [68–73]. The key determinant of phenotype is related to the dual effect of ROCK in facilitating tight junction formation and diminishing local barrier function at sites of actomyosin stress fibers [74, 75]. Barrier function in brain microvascular endothelial cells is derived from tight junctions and iBMECs do not exhibit an extensive network of F-actin stress fibers in response to shear stress. However, oxidative stress may promote stress fiber formation, at least in response to acute exposure, and thus ROCK inhibition may sensitize iBMECs to barrier disruption following oxidative stress exposure (Additional file 1: Fig. S8) [76–80]. Following additional experimentation to model acute and chronic oxidative stress schemes while maintaining 3D iBMEC model viability using ROCK inhibitor, the resultant doses (500  $\mu M$  for acute exposure, 100  $\mu M$  for chronic exposure) are on the lower end of the range explored in 2D, but remain aligned with the general regimes of dysfunction explored in aforementioned studies [53–56]. Most importantly, our study of acute exposure to oxidative stress highlights the additional dynamics of antioxidant and recovery processes in a dose-dependent manner, incorporating concentration as well as exposure time, which resulted in unique dysfunctional pathways observed in our 3D tissue-engineered BBB model.

In homeostatic conditions, ROS are continuously generated in cells but are regulated by intrinsic antioxidants and scavengers, key among them superoxide dismutase, catalases, and vitamins [2]. These agents remove or neutralize ROS from their targets and it is when these systems are overwhelmed that the state of oxidative stress, or more specifically, oxidative distress, is reached. The capacity for this counter regulation is site-specific to the tissue and cell type, and the brain vasculature is typically

more susceptible to oxidative stress damage due to its many unique sources of ROS [26]. These intrinsic regulatory drivers may account for some of the time-dependent recovery that is reflected in TEER measurements. In acute exposure to  $H_2O_2$ , there is a brief increase in TEER over 2–4 days after initial exposure, which may account for some antioxidant capacity that rebounds after the removal of the initial perturbation. However, there is a long-term effect of the acute exposure that ultimately reduces TEER ( $<500 \Omega \text{ cm}^2$ ), which may indicate the lag time between the activity of the antioxidant systems and molecular accumulation of ROS beyond the initial capacity.

Oxidative stress induced three types of defects in 3D tissue-engineered iBMEC microvessels: delaminations, focal leaks, and combined focal leak/delaminations. In the human BBB, there are three potential downstream effects demonstrated by these defects: (1) loss of cell–cell junctions, (2) loss of BMEC adhesion to basement membrane, and (3) cell loss due to cytotoxicity. Junctional disruption results in the loss of paracellular barrier function and the leakage of blood components that can contribute to neuroinflammation in brain disease. In the microvessel model, the presence of transient focal leaks identified sites of local junction disruption. In contrast, loss of BMEC adhesion results in small regions of vascular delamination. These delaminations may lead to disrupted local flow patterns that can additionally affect endothelial function, and this downstream effect may be independent or in combination with loss of cell–cell junctions [81]. Lastly,  $H_2O_2$  results in cytotoxicity when the dose approaches the limit of complete cell viability in the system—resulting in the most susceptible cells undergoing cell death. In the absence of a wound healing response from the surrounding cells, the loss will similarly result in transient focal leaks [82]. However, further increases in dose will affect a greater population of endothelial cells (as susceptible cells are expected to be randomly distributed, these defects should also be accordingly distributed) that allows cell loss to propagate, forming larger defects.

While all defect types were observed during both acute and chronic oxidative stress, combined focal leak/delaminations were most prevalent under acute conditions. Acute oxidative stress profiles are associated with primary injuries such as traumatic brain injuries or reperfusion following ischemia, which can result in more significant vascular rarefaction [83, 84], of which a primary event can be significant cell loss and inflammation, analogous to the combined focal leak/delaminations reported here. On the other hand, chronic

oxidative stress profiles are associated with neurodegenerative diseases that present clinically following accumulation of various sites of damage, typically at the cellular level [85–88]. This difference in defect types observed here emphasizes unique pathways of dysfunction between chronic and acute exposure to oxidative stress, which was supported by bulk RNA-sequencing analysis, followed by functional and protein-level confirmation. Cell turnover is similarly impacted by acute and chronic oxidative stress, but primarily driven by negative regulation of mitosis in acute conditions and by increases in apoptosis in chronic conditions. Immune cell adhesion is increased in both conditions; however, in response to acute oxidative stress, immune cells were more likely to adhere near structural defects, while in response to chronic oxidative stress, most of the adherent immune cells were unassociated with visible defects. This may indicate that the mechanisms for increased immune cell adhesion are different in acute and chronic oxidative stress exposure, and depend on the predominant type of structural defect—acute exposure may initiate increased immune cell adhesion due to changes in fluid dynamics surrounding delaminated defects, while chronic exposure may rely on other etiologies, e.g., adhesion molecule expression. By analogy, plaque build-up is associated with disrupted flow patterns at bifurcations and junctions [89, 90]. Future work in quantifying flow patterns and spatially specific protein-level assessment will be necessary to support this hypothesis, as the local nature of structural defects indicates that global changes may not reflect the true, heterogeneous nature of BBB dysfunction.

Tissue-engineered models of the BBB enable independent control of biological variables, which is important in understanding the systemic, blood-derived impact of oxidative stress in the progression of brain disease and injury. The additional contributions of local, tissue-derived oxidative stress, for example in response to aging or plaque formation in neurodegenerative disease, could be multiplexed with this model in future work to better understand the combined effects of blood- and brain-derived oxidative stress on the BBB. Since co-culture with other cell types and matrix stiffness can alter the characteristics of iBMEC microvessels, we hypothesize that these engineering design choices could also augment the response to oxidative stress (91, 92), which could be explored in future work. Our continued understanding of structural and biological changes to the BBB, which is closely linked with severe disease, will also allow investigation of strategies for recovery or prevention of these changes, with the goal of improving clinical outcomes.

## Conclusions

To match the dynamic nature of oxidant exposure mediated by the BBB during injury and disease, we studied both chronic and acute exposure to H<sub>2</sub>O<sub>2</sub> and their effect on barrier function and pathological cell processes. The influence of concentration and exposure time highlighted the dose-dependent nature of the response of iBMEC monolayers to oxidative stress. The application of these oxidative stress profiles in 3D microvessel models highlighted the localization of barrier disruption, resulting in distinct, discrete defect categories (focal leaks, delaminations, and combination focal leak/delaminations) with unique distributions based on oxidative stress dose. These were similarly linked to other functional changes under oxidative stress that are unique to each profile, particularly in cell turnover and immune cell adhesion. These functional differences emphasize the importance of appropriate dynamic modeling in the study of disease state or injury. Detailed understanding of the local changes to BBB function under oxidative stress, or other stressors associated with neurodegenerative disease and injury, is key to mapping the multiple etiologies of disease symptomology and designing appropriate interventions to improve outcomes after diagnosis or trauma.

## Abbreviations

ROS: Reactive oxygen species; H<sub>2</sub>O<sub>2</sub>: Hydrogen peroxide; NDD: Neurodegenerative disease; BBB: Blood–brain barrier; iBMEC: Induced brain microvascular endothelial-like cells; TEER: Transendothelial electrical resistance; PDMS: Polydimethylsiloxane; ROCK: Rho-associated protein kinase; LY: Lucifer yellow; RNA: Ribonucleic acid; DEG: Differentially expressed gene; GSEA: Gene set enrichment analysis.

## Supplementary Information

The online version contains supplementary material available at <https://doi.org/10.1186/s12987-022-00327-x>.

**Additional file 1: Figure S1.** Longevity of hydrogen peroxide in cell culture media. **Figure S2.** TEER, cell counts and ROS visualization. **Figure S3.** Dissolved oxygen levels in iBMEC microvessel perfusates. **Figure S4.** Dependence of sensitivity to oxidative stress on baseline TEER values of iBMECs. **Figure S5.** Maintained Lucifer yellow permeability in confluent regions of iBMEC microvessel models exposed to H<sub>2</sub>O<sub>2</sub>. **Figure S6.** Expanded RNA-sequencing pathway analysis results. **Figure S7.** Expanded pathway analysis of antioxidant stress genes and reactive oxygen species response genes. **Figure S8.** Stress fiber formation under oxidative stress. **Figure S9.** Adhesion molecule expression in response to oxidative stress. Supplemental materials and methods.

## Acknowledgements

This work was supported by DTRA (HDTRA1-15-1-0046) and NIH (R01NS106008 and R61HL154252).

## Author contributions

TDC conceptualized and carried out experiments, conducted formal analysis, and wrote, reviewed, and edited the manuscript. RML conceptualized and carried out experiments, assisted with formal analysis, and reviewed and edited

the manuscript. ZG, RY, RJ, and GNG carried out experiments. PCS conceptualized experiments, supervised the trajectory of investigation, reviewed and edited the manuscript, and acquired funding. All authors read and approved the final manuscript.

## Availability of data and materials

All data associated with this study are available in the main text or the supplementary materials. The raw data required to reproduce these findings are available from the corresponding author. RNA sequencing data is available in NCBI's GEO (Accession Number GSE193887).

## Declarations

### Competing interests

The authors declare no competing interests.

### Author details

<sup>1</sup>Institute for Nanobiotechnology, Johns Hopkins University, 100 Croft Hall, 3400 North Charles Street, Baltimore, MD, USA. <sup>2</sup>Department of Biomedical Engineering, Johns Hopkins University, Baltimore, MD, USA. <sup>3</sup>Department of Applied Mathematics and Statistics, Johns Hopkins University, Baltimore, MD, USA. <sup>4</sup>Department of Materials Science and Engineering, Johns Hopkins University, Baltimore, MD, USA.

Received: 17 November 2021 Accepted: 4 April 2022

Published online: 12 May 2022

## References

- Schieber M, Chandel NS. ROS function in redox signaling and oxidative stress. *Curr Biol*. 2014;24(10):R453–62.
- Xian D, Song J, Yang L, Xiong X, Lai R, Zhong J. Emerging roles of redox-mediated angiogenesis and oxidative stress in dermatoses. *Oxid Med Cell Longev*. 2019;2019:1–14.
- Martínez-Reyes I, Cuezva JM (2014) The H<sup>+</sup>-ATP synthase: a gate to ROS-mediated cell death or cell survival. *Biochim Biophys Acta*. 1837;7:1099–112.
- Auten RL, Davis JM. Oxygen toxicity and reactive oxygen species: the devil is in the details. *Pediatr Res*. 2009;66(2):121–7.
- Golden TR, Hinerfeld DA, Melov S. Oxidative stress and aging: beyond correlation. *Aging Cell*. 2002;1(2):117–23.
- Al-Gubory KH. Environmental pollutants and lifestyle factors induce oxidative stress and poor prenatal development. *Reprod Biomed Online*. 2014;29(1):17–31.
- Carraro E, Schilirò T, Biorci F, Romanazzi V, Degan R, Buonocore D, et al. Physical activity, lifestyle factors and oxidative stress in middle age healthy subjects. *Int J Environ Res Public Health*. 2018;15(6):1152.
- Barnham KJ, Masters CL, Bush AI. Neurodegenerative diseases and oxidative stress. *Nat Rev Drug Discov*. 2004;3(3):205–14.
- Lin MT, Beal MF. Mitochondrial dysfunction and oxidative stress in neurodegenerative diseases. *Nature*. 2006;443(7113):787–95.
- Simonian NA, Coyle JT. Oxidative stress in neurodegenerative diseases. *Annu Rev Pharmacol Toxicol*. 1996;36(1):83–106.
- Carvalho C, Moreira PI. Oxidative stress: a major player in cerebrovascular alterations associated to neurodegenerative events. *Front Physiol*. 2018. <https://doi.org/10.3389/fphys.2018.00806>.
- Praticò D, Clark CM, Liun F, Lee VYM, Trojanowski JQ. Increase of brain oxidative stress in mild cognitive impairment. *Arch Neurol*. 2002;59(6):972.
- Niedzielska E, Smaga I, Gawlik M, Moniczewski A, Stankowicz P, Pera J, et al. Oxidative stress in neurodegenerative diseases. *Mol Neurobiol*. 2015;53(6):4094–125.
- Chang T-C, Chen Y-C, Huang Y-C, Lin W-C, Lu C-H. Systemic oxidative stress and cognitive function in Parkinson's disease with different PWMH or DWMH lesions. *BMC Neurol*. 2021. <https://doi.org/10.1186/s12883-020-02037-z>.
- Liguori I, Russo G, Curcio F, Bulli G, Aran L, Della-Morte D, et al. Oxidative stress, aging, and diseases. *Clin Interv Aging*. 2018;13:757–72.

16. Luceri C, Bigagli E, Femia AP, Caderni G, Giovannelli L, Lodovici M. Aging related changes in circulating reactive oxygen species (ROS) and protein carbonyls are indicative of liver oxidative injury. *Toxicol Rep.* 2018;5:141–5.
17. Rao X, Zhong J, Brook RD, Rajagopalan S. Effect of particulate matter air pollution on cardiovascular oxidative stress pathways. *Antioxid Redox Signal.* 2018;28(9):797–818.
18. Block ML, Calderón-Garcidueñas L. Air pollution: mechanisms of neuroinflammation and CNS disease. *Trends Neurosci.* 2009;32(9):506–16.
19. de la Torre JC. The vascular hypothesis of Alzheimer's disease: bench to bedside and beyond. *Neurodegener Dis.* 2010;7(1–3):116–21.
20. Hsueh H, Kastin AJ, Mishra PK, Pan W. C-reactive protein increases BBB permeability: implications for obesity and neuroinflammation. *Cell Physiol Biochem.* 2012;30(5):1109–19.
21. Madamanchi NR, Vendrov A, Runge MS. Oxidative stress and vascular disease. *Arterioscler Thromb Vasc Biol.* 2005;25(1):29–38.
22. Persidsky Y, Ramirez SH, Haorah J, Kanmogne GD. Blood–brain barrier: structural components and function under physiologic and pathologic conditions. *J Neuroimmune Pharmacol.* 2006;1(3):223–36.
23. Wong AD, Ye M, Levy AF, Rothstein JD, Bergles DE, Searson PC. The blood–brain barrier: an engineering perspective. *Front Neuroeng.* 2013. <https://doi.org/10.3389/fneng.2013.00007>.
24. Carrano A, Hoozemans JJM, van der Vies SM, van Horsen J, de Vries HE, Rozemuller AJM. Neuroinflammation and blood–brain barrier changes in capillary amyloid angiopathy. *Neurodegener Dis.* 2012;10(1–4):329–31.
25. Abdul-Muneer PM, Schuetz H, Wang F, Skotak M, Jones J, Gorantla S, et al. Induction of oxidative and nitrosative damage leads to cerebrovascular inflammation in an animal model of mild traumatic brain injury induced by primary blast. *Free Radical Biol Med.* 2013;60:282–91.
26. van Leeuwen E, Hampton MB, Smyth LCD. Redox signalling and regulation of the blood–brain barrier. *Int J Biochem Cell Biol.* 2020. <https://doi.org/10.1016/j.biocel.2020.105794>.
27. Drake J. Oxidative stress precedes fibrillar deposition of Alzheimer's disease amyloid  $\beta$ -peptide (1–42) in a transgenic *Caenorhabditis elegans* model. *Neurobiol Aging.* 2003;24(3):415–20.
28. Matsumura A, Emoto MC, Suzuki S, Iwahara N, Hisahara S, Kawamata J, et al. Evaluation of oxidative stress in the brain of a transgenic mouse model of Alzheimer disease by in vivo electron paramagnetic resonance imaging. *Free Radic Biol Med.* 2015;85:165–73.
29. Anasooya Shaji C, Robinson BD, Yeager A, Beeram MR, Davis ML, Isbell CL, et al. The Tri-phasic role of hydrogen peroxide in blood–brain barrier endothelial cells. *Sci Rep.* 2019. <https://doi.org/10.1038/s41598-018-36769-3>.
30. Wilson EH, Ullen A, Singewald E, Konya V, Fauler G, Reicher H, et al. Myeloperoxidase-derived oxidants induce blood–brain barrier dysfunction in vitro and in vivo. *PLoS ONE.* 2013. <https://doi.org/10.1371/journal.pone.0064034>.
31. Lushchak VI. Glutathione homeostasis and functions: potential targets for medical interventions. *J Amino Acids.* 2012;2012:1–26.
32. Manzanero S, Santro T, Arumugam TV. Neuronal oxidative stress in acute ischemic stroke: sources and contribution to cell injury. *Neurochem Int.* 2013;62(5):712–8.
33. Kishimoto M, Suenaga J, Takase H, Araki K, Yao T, Fujimura T, et al. Oxidative stress-responsive apoptosis inducing protein (ORAIP) plays a critical role in cerebral ischemia/reperfusion injury. *Sci Rep.* 2019. <https://doi.org/10.1038/s41598-019-50073-8>.
34. Houben MJM, Moonen HJJ, van Schooten FJ, Hageman GJ. Telomere length assessment: biomarker of chronic oxidative stress? *Free Radic Biol Med.* 2008;44(3):235–46.
35. Solleiro-Villavicencio H, Rivas-Arancibia S. Effect of chronic oxidative stress on neuroinflammatory response mediated by CD4+T cells in neurodegenerative diseases. *Front Cell Neurosci.* 2018. <https://doi.org/10.3389/fncel.2018.00114>.
36. Quilty MC, King AE, Gai WP, Pountney DL, West AK, Vickers JC, et al. Alpha-synuclein is upregulated in neurons in response to chronic oxidative stress and is associated with neuroprotection. *Exp Neurol.* 2006;199(2):249–56.
37. Bisht K, Sharma K, Tremblay M-È. Chronic stress as a risk factor for Alzheimer's disease: roles of microglia-mediated synaptic remodeling, inflammation, and oxidative stress. *Neurobiol Stress.* 2018;9:9–21.
38. Matthesen I, Vulgaris D, Nikolakopoulou P, Winkler TE, Herland A. Continuous monitoring reveals protective effects of N-acetylcysteine amide on an isogenic microphysiological model of the neurovascular unit. *Small.* 2021;17(32):2101785.
39. Linville RM, Sklar MB, Grifno GN, Nerenberg RF, Zhou J, Ye R, et al. Three-dimensional microenvironment regulates gene expression, function, and tight junction dynamics of iPSC-derived blood–brain barrier microvessels. *bioRxiv.* 2021. <https://doi.org/10.1101/2021.08.27.457975>.
40. Linville RM, DeStefano JG, Sklar MB, Xu Z, Farrell AM, Bogorad MI, et al. Human iPSC-derived blood–brain barrier microvessels: validation of barrier function and endothelial cell behavior. *Biomaterials.* 2019;190–191:24–37.
41. DeStefano JG, Jamieson JJ, Linville RM, Searson PC. Benchmarking in vitro tissue-engineered blood–brain barrier models. *Fluids Barriers CNS.* 2018. <https://doi.org/10.1186/s12987-018-0117-2>.
42. Workman MJ, Svendsen CN. Recent advances in human iPSC-derived models of the blood–brain barrier. *Fluids Barriers CNS.* 2020. <https://doi.org/10.1186/s12987-020-00191-7>.
43. Lippmann ES, Azarin SM, Palecek SP, Shusta EV. Commentary on human pluripotent stem cell-based blood–brain barrier models. *Fluids Barriers CNS.* 2020. <https://doi.org/10.1186/s12987-020-00222-3>.
44. Lippmann ES, Azarin SM, Kay JE, Nessler RA, Wilson HK, Al-Ahmad A, et al. Derivation of blood–brain barrier endothelial cells from human pluripotent stem cells. *Nat Biotechnol.* 2012;30(8):783–91.
45. Misteli T, McQuin C, Goodman A, Chernyshev V, Kamentsky L, Cimini BA, et al. Cell Profiler 3.0: next-generation image processing for biology. *PLOS Biol.* 2018. <https://doi.org/10.1371/journal.pbio.2005970>.
46. Katt ME, Linville RM, Mayo LN, Xu ZS, Searson PC. Functional brain-specific microvessels from iPSC-derived human brain microvascular endothelial cells: the role of matrix composition on monolayer formation. *Fluid Barriers CNS.* 2018. <https://doi.org/10.1186/s12987-018-0092-7>.
47. Newby D, Marks L, Lyall F. Dissolved oxygen concentration in culture medium: assumptions and pitfalls. *Placenta.* 2005;26(4):353–7.
48. Liao Y, Smyth GK, Shi W. The R package Rsubread is easier, faster, cheaper and better for alignment and quantification of RNA sequencing reads. *Nucleic Acids Res.* 2019;47(8):e47.
49. Love MI, Huber W, Anders S. Moderated estimation of fold change and dispersion for RNA-seq data with DESeq2. *Genome Biol.* 2014. <https://doi.org/10.1186/s13059-014-0550-8>.
50. Chen EY, Tan CM, Kou Y, Duan Q, Wang Z, Meirelles G, et al. Enrichr: interactive and collaborative HTML5 gene list enrichment analysis tool. *BMC Bioinform.* 2013. <https://doi.org/10.1186/1471-2105-14-128>.
51. Wickham H. *ggplot2: elegant graphics for data analysis.* New York: Springer-Verlag; 2016.
52. Gille JJP, Joenje H. Cell culture models for oxidative stress: superoxide and hydrogen peroxide versus normobaric hyperoxia. *Mutat Res.* 1992;275(3–6):405–14.
53. Hyslop PA, Zhang Z, Pearson DV, Phebus LA. Measurement of striatal H<sub>2</sub>O<sub>2</sub> by microdialysis following global forebrain ischemia and reperfusion in the rat: correlation with the cytotoxic potential of H<sub>2</sub>O<sub>2</sub> in vitro. *Brain Res.* 1995;671(2):181–6.
54. Kondrashov VA. Comparative toxicity of hydrogen peroxide vapors via inhalatory and skin routes of exposure. *Gig Tr Prof Zabol.* 1977;10:22–5.
55. ECETOC. Hydrogen peroxide, Special Report No. 10. Brussels. 1996.
56. EU. Risk assessment report, hydrogen peroxide. Brussels. 2003.
57. Linville RM, DeStefano JG, Nerenberg RF, Grifno GN, Ye R, Gallagher E, et al. Long-term cryopreservation preserves blood–brain barrier phenotype of iPSC-derived brain microvascular endothelial cells and three-dimensional microvessels. *Mol Pharm.* 2020;17(9):3425–34.
58. Toborek M, Roe K, Orillo B, Verma S. West Nile Virus-induced cell adhesion molecules on human brain microvascular endothelial cells regulate leukocyte adhesion and modulate permeability of the in vitro blood–brain barrier model. *PLoS ONE.* 2014. <https://doi.org/10.1371/journal.pone.0102598>.
59. Rossi B, Angiari S, Zenaro E, Budui SL, Constantin G. Vascular inflammation in central nervous system diseases: adhesion receptors controlling leukocyte–endothelial interactions. *J Leukoc Biol.* 2010;89(4):539–56.
60. Zenaro E, Rossi B, Angiari S, Constantin G. Use of imaging to study leukocyte trafficking in the central nervous system. *Immunol Cell Biol.* 2013;91(4):271–80.
61. Nishihara H, Gastfriend BD, Soldati S, Perriot S, Mathias A, Sano Y, et al. Advancing human induced pluripotent stem cell-derived blood–brain



- barrier models for studying immune cell interactions. *FASEB J*. 2020;34(12):16693–715.
62. Ratan RR, Murphy TH, Baraban JM. Rapid communication: oxidative stress induces apoptosis in embryonic cortical neurons. *J Neurochem*. 2008;62(1):376–9.
  63. Kimura Y, Kimura H. Hydrogen sulfide protects neurons from oxidative stress. *FASEB J*. 2004;18(10):1165–7.
  64. Varadarajan S, Yatin S, Akseanova M, Butterfield DA. Review: Alzheimer's amyloid  $\beta$ -peptide-associated free radical oxidative stress and neurotoxicity. *J Struct Biol*. 2000;130(2–3):184–208.
  65. Sies H. Role of metabolic H<sub>2</sub>O<sub>2</sub> generation. *J Biol Chem*. 2014;289(13):8735–41.
  66. Sies H. Hydrogen peroxide as a central redox signaling molecule in physiological oxidative stress: oxidative eustress. *Redox Biol*. 2017;11:613–9.
  67. Linville RM, Arevalo D, Maressa JC, Zhao N, Searson PC. Three-dimensional induced pluripotent stem-cell models of human brain angiogenesis. *Microvasc Res*. 2020. <https://doi.org/10.1016/j.mvr.2020.104042>.
  68. Park J-C, Baik SH, Han S-H, Cho HJ, Choi H, Kim HJ, et al. Annexin A1 restores  $\beta$ 1-42-induced blood-brain barrier disruption through the inhibition of RhoA-ROCK signaling pathway. *Aging Cell*. 2017;16(1):149–61.
  69. Fujii M, Duris K, Altay O, Soejima Y, Sherchan P, Zhang JH. Inhibition of Rho kinase by hydroxyfasudil attenuates brain edema after subarachnoid hemorrhage in rats. *Neurochem Int*. 2012;60(3):327–33.
  70. Grothaus JS, Ares G, Yuan C, Wood DR, Hunter CJ. Rho kinase inhibition maintains intestinal and vascular barrier function by upregulation of occludin in experimental necrotizing enterocolitis. *Am J Physiol Gastrointest Liver Physiol*. 2018;315(4):G514–28.
  71. Okumura N, Kinoshita S, Koizumi N. Application of Rho kinase inhibitors for the treatment of corneal endothelial diseases. *J Ophthalmol*. 2017;2017:1–8.
  72. Connon CJ, Pipparelli A, Arsenijevic Y, Thuret G, Gain P, Nicolas M, et al. ROCK inhibitor enhances adhesion and wound healing of human corneal endothelial cells. *PLoS ONE*. 2013. <https://doi.org/10.1371/journal.pone.0062095>.
  73. Walsh SV, Hopkins AM, Chen J, Narumiya S, Parkos CA, Nusrat A. Rho kinase regulates tight junction function and is necessary for tight junction assembly in polarized intestinal epithelia. *Gastroenterology*. 2001;121(3):566–79.
  74. van Nieuw Amerongen GP, Beckers CML, Achekar ID, Zeeman S, Musters RJP, van Hinsbergh VWM. Involvement of Rho kinase in endothelial barrier maintenance. *Arterioscler Thromb Vasc Biol*. 2007;27(11):2332–9.
  75. Van Itallie CM, Fanning AS, Bridges A, Anderson JM, Mostov K. ZO-1 stabilizes the tight junction solute barrier through coupling to the perijunctional cytoskeleton. *Mol Biol Cell*. 2009;20(17):3930–40.
  76. Faley SL, Neal EH, Wang JX, Bosworth AM, Weber CM, Balotin KM, et al. iPSC-derived brain endothelium exhibits stable, long-term barrier function in perfused hydrogel scaffolds. *Stem Cell Reports*. 2019;12(3):474–87.
  77. DeStefano JG, Xu ZS, Williams AJ, Yimam N, Searson PC. Effect of shear stress on iPSC-derived human brain microvascular endothelial cells (dhBMECs). *Fluids Barriers CNS*. 2017. <https://doi.org/10.1186/s12987-017-0068-z>.
  78. Reinitz A, DeStefano J, Ye M, Wong AD, Searson PC. Human brain microvascular endothelial cells resist elongation due to shear stress. *Microvasc Res*. 2015;99:8–18.
  79. Wang YI, Abaci HE, Shuler ML. Microfluidic blood–brain barrier model provides in vivo-like barrier properties for drug permeability screening. *Biotechnol Bioeng*. 2016;114(1):184–94.
  80. Ye M, Sanchez HM, Hultz M, Yang Z, Bogorad M, Wong AD, et al. Brain microvascular endothelial cells resist elongation due to curvature and shear stress. *Sci Rep*. 2014. <https://doi.org/10.1038/srep04681>.
  81. Bouhrira N, DeOre BJ, Sazer DW, Chiaradia Z, Miller JS, Galie PA. Disturbed flow disrupts the blood–brain barrier in a 3D bifurcation model. *Biofabrication*. 2020. <https://doi.org/10.1088/1758-5090/ab5898>.
  82. Linville RM, DeStefano JG, Sklar MB, Chu C, Walczak P, Searson PC. Modeling hyperosmotic blood–brain barrier opening within human tissue-engineered in vitro brain microvessels. *J Cereb Blood Flow Metab*. 2019;40(7):1517–32.
  83. Lu X, Dong J, Zheng D, Li X, Ding D, Xu H. Reperfusion combined with intraarterial administration of resveratrol-loaded nanoparticles improved cerebral ischemia–reperfusion injury in rats. *Nanomedicine*. 2020. <https://doi.org/10.1016/j.nano.2020.102208>.
  84. Obadia N, Lessa MA, Daliry A, Silveiras RR, Gomes F, Tibiriçá E, et al. Cerebral microvascular dysfunction in metabolic syndrome is exacerbated by ischemia–reperfusion injury. *BMC Neurosci*. 2017. <https://doi.org/10.1186/s12868-017-0384-x>.
  85. Nguyen MT, Lue H, Kleemann R, Thiele M, Tolle G, Finkelmeier D, et al. The cytokine macrophage migration inhibitory factor reduces pro-oxidative stress-induced apoptosis. *J Immunol*. 2003;170(6):3337–47.
  86. Gill R, Tsung A, Billiar T. Linking oxidative stress to inflammation: Toll-like receptors. *Free Radic Biol Med*. 2010;48(9):1121–32.
  87. Shackelford RE, Kaufmann WK, Paules RS. Oxidative stress and cell cycle checkpoint function. Both Drs. Paules and Kaufmann received their doctoral degrees in Experimental Pathology from the University of North Carolina at Chapel Hill School of Medicine (in 1984 and 1979, respectively). *Free Radic Biol Med*. 2000;28(9):1387–404.
  88. Klein JA, Ackerman SL. Oxidative stress, cell cycle, and neurodegeneration. *J Clin Invest*. 2003;111(6):785–93.
  89. Warboys CM, Amini N, Luca Ad, Evans PC. The role of blood flow in determining the sites of atherosclerotic plaques. *F1000 Med Rep*. 2011. <https://doi.org/10.3410/M3-5>.
  90. Ravensbergen J, Ravensbergen JW, Krijger JKB, Hillen B, Hoogstraten HW. Localizing role of hemodynamics in atherosclerosis in several human vertebralbasilar junction geometries. *Arterioscler Thromb Vasc Biol*. 1998;18(5):708–16.
  91. Jamieson JJ, Linville RM, Ding YY, Gerech S, Searson PC. Role of iPSC-derived pericytes on barrier function of iPSC-derived brain microvascular endothelial cells in 2D and 3D. *Fluids Barriers CNS*. 2019. <https://doi.org/10.1186/s12987-019-0136-7>.
  92. Grifno GN, Farrell AM, Linville RM, Arevalo D, Kim JH, Gu L, et al. Tissue-engineered blood–brain barrier models via directed differentiation of human induced pluripotent stem cells. *Sci Rep*. 2019. <https://doi.org/10.1038/s41598-019-50193-1>.

## Publisher's Note

Springer Nature remains neutral with regard to jurisdictional claims in published maps and institutional affiliations.

Ready to submit your research? Choose BMC and benefit from:

- fast, convenient online submission
- thorough peer review by experienced researchers in your field
- rapid publication on acceptance
- support for research data, including large and complex data types
- gold Open Access which fosters wider collaboration and increased citations
- maximum visibility for your research: over 100M website views per year

At BMC, research is always in progress.

Learn more [biomedcentral.com/submissions](https://biomedcentral.com/submissions)

